Modeling the Magnetic Field Radiated from a Ferrite Rod Antenna for Mining Proximity Detection Systems

Chenming Zhou, Jingcheng Li, and Jacob Carr
Pittsburgh Mining Research Division (PMRD)
National Institute for Occupational Safety and Health (NIOSH), Pittsburgh, PA 15236, USA

Abstract— Magnetic Proximity Detection Systems (PDSs) are widely used in the mining industry for protecting mine workers from striking and pinning injuries when they work in close proximity to heavy machines such as Continuous Mining Machines (CMMs) and mobile haulage equipment. Researchers at the National Institute for Occupational Safety and Health (NIOSH) have conducted extensive measurement-based studies to investigate the performance of PDSs. To enable further investigation of scenarios for which physical measurements are impractical, a simulation-based approach is needed. In this paper, we present the development and validation of a simulation-based approach in which FEKO is used to model the magnetic field radiated from a ferrite rod antenna used in a commercial PDS. FEKO-based simulation results are compared to both analytical results and physical measurements and show good agreement. In addition, the major factors (including current, frequency, antenna length, antenna radius, number of turns and ferrite permeability) for controlling the magnetic field and thus the performance of a magnetic PDS are analyzed. This paper confirms that FEKO can accurately model the magnetic field radiated from a PDS antenna. The findings of the paper will help researchers and PDS manufacturers to better understand the magnetic field distribution of PDSs and design optimized PDSs that are more robust to underground mining environments.

1. INTRODUCTION

Underground mine workers often need to work in close proximity to heavy machines such as Continuous Mining Machines (CMMs) and mobile haulage equipment. Due to the space and visibility limitations underground, these mine workers can be struck, crushed, or pinned by the heavy machines near them which can lead to severe injuries and fatalities. According to the accident injuries data set published by the Mine Safety and Health Administration (MSHA) [1], there have been 44 fatalities in which a miner was crushed by a remote-control CMM since 1984. In addition, there have been 34 fatal accidents involving mobile haulage since 2000.

Proximity Detection Systems (PDSs) have been developed to prevent mine workers from striking and pinning injuries caused by heavy machines [2–4]. MSHA promulgated a regulation in 2015 requiring the use of a PDS on all CMMs except full-face machines and proposed a regulation in the same year which would require a PDS on other mobile underground equipment.

While a number of technologies including Lidar, Radar, RFID, and video can be used for mining proximity detection [5], current MSHA-approved PDSs for underground coal mines in the United States are all magnetic-field-based. As shown in Figure 1, a magnetic PDS typically includes two major components: magnetic field generators and Miner Wearable Components (MWCs). Magnetic fields are generated by injecting a high electric current to a ferrite rod antenna sealed in a generator. The magnetic field detected by an MWC varies with the distance between the MWC and the generator. In a typical PDS, multiple generators are mounted on different locations of the machine. The location/zone of an MWC relative to the machine (generators) is determined based on the field strengths measured by the MWC from different generators.

Researchers at the National Institute for Occupational Safety and Health (NIOSH) have performed extensive investigations on the magnetite PDSs in the past decades [2, 4, 6–11]. Those studies, however, were mostly measurement-based which involved measuring magnetic fields with appropriate instruments. Recently a shell-based model has been proposed for modeling the magnetic field radiated from a PDS generator [12, 13]. Again, this shell-based model is a measurement-based empirical model as the four key parameters of the model are obtained by fitting exponential curves to a series of measured magnetic field data points.

To enable further investigation of scenarios for which physical measurements are impractical, a simulation-based approach is needed. For example, it is known that wire mesh, which is commonly used in underground mines to provide surface support coverage to loose rock, can have a significant impact on the performance of a magnetic PDS. The degree to which this effect occurs is dependent on the dimensions of the underground opening. Therefore, a simulation-based approach, after being

validated, would be helpful for this research as conducting physical measurements in mine entries with controlled dimensions is not feasible.

For a simulation-based approach, identifying the right simulation tool is vitally important. Many electromagnetic (EM) simulation tools are now available for EM related research. However, most of these tools are targeted for microwave (GHz-range) applications and may not be accurate at our frequencies of interest in the kHz-range. Historically, FEKO, a full wave, method-of-moment (MoM) based simulation software, has been used for studying the magnetic field coupled to and propagating along a wire at the medium frequency (MF) band (300 kHz–3 MHz) [14–17]. It has also been used in Through-the-Earth (TTE) communication research for modeling the magnetic field attenuation through the earth at the Low Frequency (LF) and Extremely Low Frequency (ELF) band [18]. In this paper, we demonstrate the use of FEKO to model the magnetic field radiated from a ferrite rod antenna used in an MSHA-approved PDS operating at a frequency around 73 kHz. We validate the FEKO-based simulation approach by comparing FEKO simulated results to corresponding analytical and measured results under different scenarios.

Another contribution of this paper is that we analyze the major controlling factors of the magnetic field from a PDS. Existing PDSs in underground coal mines offer a means of warning miners or automatically disabling machine motion when they are within potentially hazardous proximity to a machine, however, system performance might not be optimized in terms of susceptibility to environmental influences. Understanding the controlling factors for system performance is critical in designing next generation PDSs that are more robust to various mining environments.

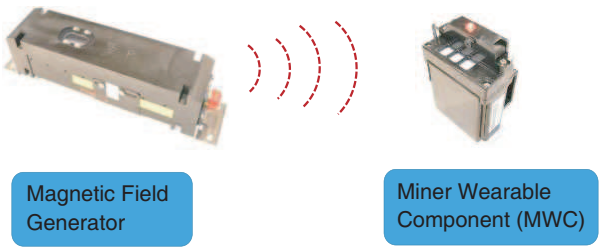

Figure 1: Two major components of a permissible magnetic PDS used in coal mines: a generator and an MWC.

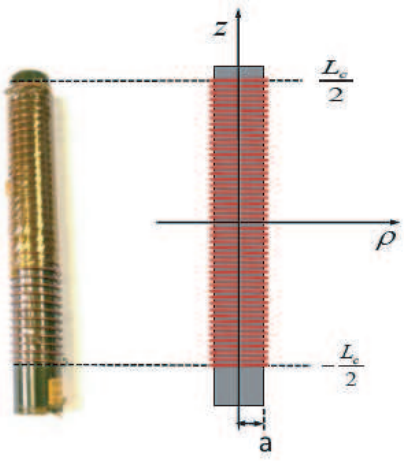

Figure 2: Geometry of a ferrite rod antenna.

2. ANALYTICAL MODELING OF MAGNETIC FIELDS GENERATED BY AN AIR COIL

To understand the controlling factors of the magnetic field generated by a ferrite rod antenna as illustrated in Figure 2, we first look at the field radiated from an air coil which has an analytical solution. We consider an N-turn solenoid with a radius of a, similar to the antenna shown in Figure 2 but without the ferrite core inside. The solenoid has a length of L_c and carries a constant current I. The origin of the coordinate system is oriented in the center of the solenoid. The magnetic field at an arbitrary position $P(\rho, z)$ can be viewed as the superposition of the magnetic fields generated from N parallel loops. It is known that the vector potential of the n-th loop located at $z = z_n$ has only a single component in the ϕ direction that can be expressed as [19–22]:

$$A_\phi^n(\rho, z, a, z_n, I) = \frac{\mu_0 I}{\pi\varsigma}\sqrt{\frac{a}{\rho}}\left[\left(1 - \frac{1}{2}\varsigma^2\right)K(\varsigma) - E(\varsigma)\right] \tag{1}$$

where

$$\varsigma = \sqrt{\frac{4a\rho}{(a+\rho)^2 + (z - z_n)^2}} \tag{2}$$

In (1), $K(\varsigma)$ and $E(\varsigma)$ are complete elliptic integrals of the first and second kind, respectively. $K(\varsigma)$ and $E(\varsigma)$ are given by:

$$\begin{aligned} K(\varsigma) &= \int_0^{\frac{\pi}{2}} \frac{d\theta}{\sqrt{1-\varsigma^2\sin^2\theta}} = \frac{\pi}{2}\sum_{m=0}^{\infty}\left(\frac{(2m)!}{2^{2m}(m!)^2}\right)^2\varsigma^{2m} \\ E(\varsigma) &= \int_0^{\frac{\pi}{2}} \sqrt{1-\varsigma^2\sin^2\theta}d\theta = \frac{\pi}{2}\sum_{m=0}^{\infty}\left(\frac{(2m)!}{2^{2m}(m!)^2}\right)^2\frac{\varsigma^{2m}}{1-2m} \end{aligned} \tag{3}$$

By carrying out the curl in the cylindrical coordinate, the components of the magnetic flux density (B-field) radiated from the n-th loop then can be obtained as [20]:

$$\begin{aligned} B_\rho^n(\rho,z,a,z_n,I) &= \frac{\mu_0 I}{2\pi}\frac{z-z_n}{\rho\sqrt{(a+\rho)^2+(z-z_n)^2}} \\ &\quad\cdot\left[-K(\varsigma)+\frac{a^2+\rho^2+(z-z_n)^2}{(a-\rho)^2+(z-z_n)^2}E(\varsigma)\right] \end{aligned} \tag{4}$$

$$\begin{aligned} B_z^n(\rho,z,a,z_n,I) &= \frac{\mu_0 I}{2\pi}\frac{1}{\sqrt{(a+\rho)^2+(z-z_n)^2}} \\ &\quad\cdot\left[K(\varsigma)+\frac{a^2-\rho^2-(z-z_n)^2}{(a-\rho)^2+(z-z_n)^2}E(\varsigma)\right] \end{aligned} \tag{5}$$

$$B_\phi^n(\rho,z,a,z_n,I) = 0 \tag{6}$$

where

$$z_n = \begin{cases} -\frac{L_c}{2}+(2n-1)\cdot\frac{L_c}{2N} & (N \text{ is even}) \\ -\frac{L_c}{2}+(n-1)\cdot\frac{L_c}{N-1} & (N \text{ is odd}) \end{cases} \tag{7}$$

As a result, the B-field of the air core has components on the radial and loop axes that can be calculated as:

$$B_\rho(\rho,z,a,N,L_c,I) = \sum_{n=1}^{N} B_\rho^n(\rho,z,a,z_n,I) \tag{8}$$

$$B_z(\rho,z,a,N,L_c,I) = \sum_{n=1}^{N} B_z^n(\rho,z,a,z_n,I) \tag{9}$$

It should be noted that (4) and (5) are general analytical formulas for calculating the B-field generated by a multi-turn loop antenna. As a result, (4) and (5) can be widely applied to different applications where loop antennas are involved. For example, in addition to proximity detection systems, the main focus of this paper, (4) and (5) can also be applied to model the B-field radiated from a loop antenna in TTE communications.

For a PDS used for mining applications, a three-axis (i.e., X, Y and Z) receiver is generally used to measure the three individual components of the B-field. The measured three-axis components are then combined to obtain the vector sum of the field which will be used for calculating location/zone of the receiver. Based on Eqs. (4)–(9), the vector sum of the B-field can be calculated as:

$$B(\rho,z,a,N,L_c,I) = \sqrt{B_\rho^2+B_z^2} \tag{10}$$

It is apparent from (10) that the following factors control the B-field radiated from a solenoid:

1. Radius (a)
2. Number of turns (N)
3. Length of the coil (L_c)
4. Current (I)

The above four factors are the major controlling factors for the magnetic field at a fixed location. In addition to these four factors, it is apparent that the magnetic field received by an MWC varies with the location of the MWC. (i.e., the parameter ρ and z). In a proximity detection application, all of the parameters except ρ and z are assumed to be constant so any measured magnetic field change can be attributed to the change of MWC location (i.e., ρ and z).

3. NUMERICAL MODELING OF MAGNETIC FIELDS BASED ON FEKO

While an analytical method provides good physical insight into the controlling factors of the field, the method is only limited to some relative simple scenarios such as an air core. For problems where complicated geometric structures are involved, an analytical solution is generally not available and thus a numerical approach would be sought. In this section, we will describe the simulation setup for calculating the B-field radiated from a ferrite rod antenna using FEKO.

Figure 3 shows a ferrite rod antenna used in a generator extracted from a commercial PDS and the corresponding FEKO model on a computer screen. The geometric parameters of the simulated antenna are chosen strictly based on the real antenna used in the commercial system and are given in Table 1. The antenna in Figure 3 uses an M25 ferrite core which is a low-loss MnZn ferrite designed for high flux power applications. The relative permeability of the ferrite rod in Table 1 is chosen based on the information provided in the data sheet of the M25 material.

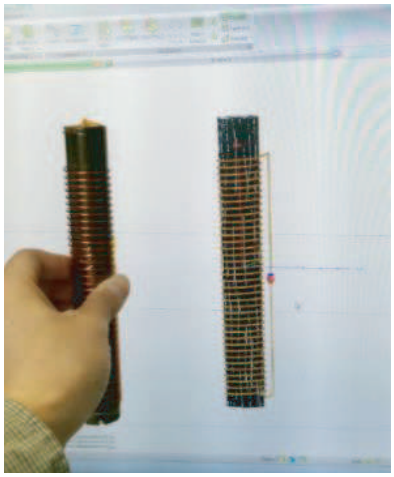

Figure 3: Photo of a ferrite rod antenna used in a commercial PDS and the corresponding FEKO model (on the right).

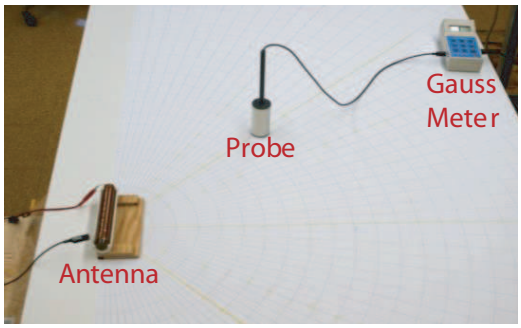

Figure 4: Experimental setup for measuring the magnetic field radiated from a ferrite rod antenna used by a commercial PDS.

Table 1: Antenna parameters.

Parameter	Value
Radius (a)	12.7 mm
Number of turns (N)	37
Length (L_c)	0.16 m
Ferrite length (L_f)	0.1905 m
Permeability (μ_r)	2500
Wire radius	0.685 mm
Frequency (f)	73.6 kHz

4. MEASUREMENT OF THE MAGNETIC FIELD

To further validate the FEKO model, measurements were carried out to characterize the B-field radiated from the ferrite rod antenna shown in Figure 3. As shown in Figure 4, the B-field was measured using a digital AC Gauss meter, IDR-200, with a three-axis probe. The antenna was excited by an RF amplifier, E&I 1020L, with a 73.6-kHz continuous sinusoid signal fed from a

signal generator (not shown in Figure 4). The current through the antenna was measured to be 3.86 A. The center of the antenna was carefully placed on the origin of a printed polar chart laid on a wood table. The probe was moved along the radial lines of the polar coordinate system at preselected angles (0°, 60°, 120°, 180°, to locate points with three targeted B-field values (i.e., 10, 110.9 and 250 mG). As a result, three independent sets of measurement points or three "shells" were obtained for which all of the points on each shell have an equal B-field value of 10, 110.9 and 250 mG, respectively.

5. RESULTS AND DISCUSSION

5.1. Comparing FEKO Modelling to Analytical Modelling

Figure 5 shows a comparison of the Z-component of the B-field which is calculated based on FEKO and the analytical method which is calculated based on (9), respectively. To better visualize the data, in Figure 5, the B-field has been plotted on a logarithmic scale and the distance on the Z axis has been normalized to the length of the coil L_c. It can be seen from Figure 5 that the FEKO-based simulation results agree well with the analytical solution. It is also shown that as expected, the value of the B-field is maximum inside the coil and remains approximately unchanged through the length of the coil, and then quickly drops outside of the coil.

Similar to Figure 5, Figure 6 shows a comparison of the B-field on the ρ axis simulated based on FEKO and the analytical method. Again, the results based on the two methods show a good agreement.

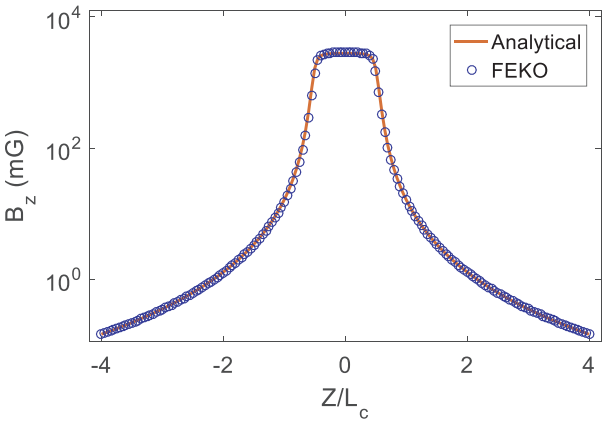

Figure 5: A comparison of the B-field (normalized with respect to the current) on the Z axis ($\rho = 0$) calculated based on FEKO and the analytical method.

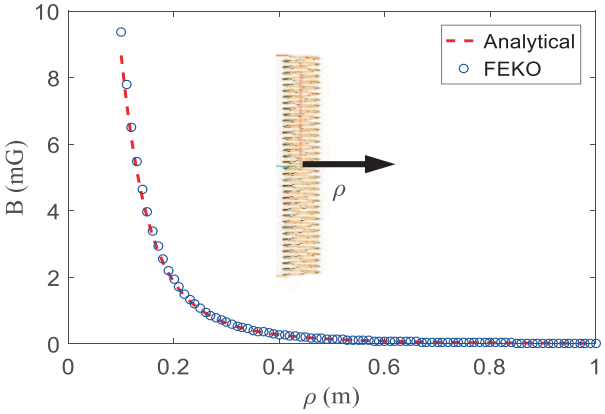

Figure 6: A comparison of the B-field (normalized with respect to the current) on the ρ axis ($z = 0$) calculated based on FEKO simulation and the anlalytical method.

5.2. Validating FEKO Modelling with Measurements

Figure 7 shows a simulated B-field distribution around a ferrite rod antenna. It is plotted based on the vector sum of the B-field calculated by FEKO using the antenna whose parameters are given in Table 1. It is a discrete contour plot where points with similar B-field strengths are grouped together and plotted with the same color. These magnetic field contours are similar to the equal magnetic field shells developed in previous NIOSH research [12, 13].

Figure 8 shows a comparison between the simulated and measured shells at different B-values. The simulated shells are plotted with a green star marker and the black circles represent the corresponding measured data. It is shown from Figure 8 that FEKO simulated shells match well with the measured shells for all three B values.

Figure 9 shows a simulated rod antenna pattern. Only the top half part of the pattern is shown here as the bottom part is expected to be the same as the top half, based on the symmetry of the antenna. Similar to equal-B shells shown in Figure 8, the antenna pattern shown in Figure 9 can be viewed as equal-R shells where every point on the shell has the same R value which is the radial distance between the observation point and the center of the antenna. Since R is the same, the B-field can be plotted against the angle to show which direction of the antenna has the maximum

field/energy. It is apparent from Figure 9 that the B-field is strongest along the antenna axis (0 and 180 degrees) and is relatively weak in the center (90 degrees). In other words, rod antennas generally have a better B-field coverage at the two ends of the antenna. As a result, unless there are other special reasons, rod antennas should be mounted horizontally rather than vertically in order to achieve the best coverage on the horizontal plane for proximity detection application.

5.3. Controlling Factor Analysis

Current (I): Based on (4) and (5), it is apparent that both z and ρ components of the B-field are proportional to current I. As a result, the vector sum of the B-field is proportional to the current. In other words, we have:

$$B(\rho, z, a, N, L_c, I) = C_1(\rho, z, N, L_c, a) \cdot I \tag{11}$$

where $C_1(\rho, z, N, L_c, a)$ is a measurable constant determined by parameters including ρ, z, N, L_c, and a.

It should be noted that in a practical application the current I might be affected by some other system parameters such as temperature and the impedance of the antenna. This is because the signal source is generally a voltage source rather than a current source. In other words, the current varies with other controlling factors, such as the number of turns, radius, and the length of the coil which directly affect the impedance of the coil. In addition, some environmental factors, such

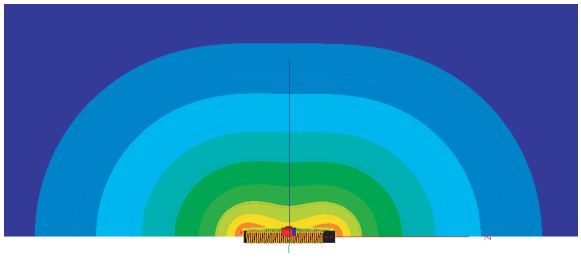

Figure 7: Simulated B-field contours around a ferrite rod antenna.

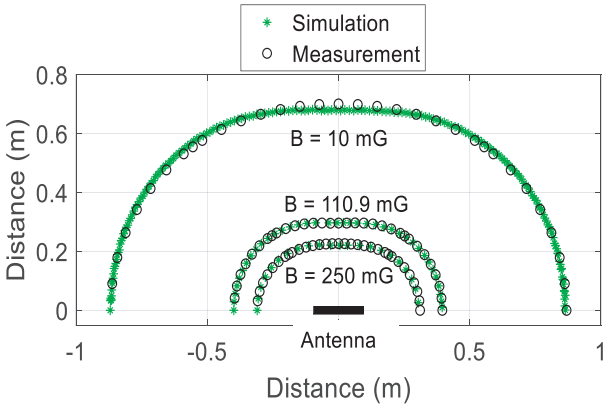

Figure 8: A comparison of the simulated and measured equal B-field shells. On each shell, the vector sum of the three-axis magnetic field has the same value of 10 mG, 110.9 mG and 250 mG, respectively.

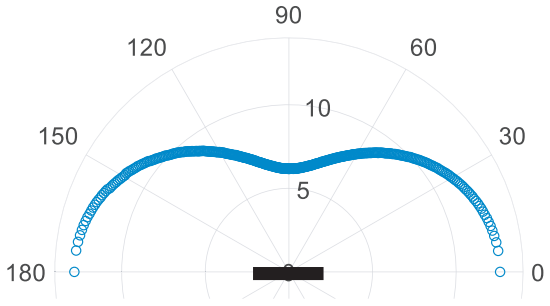

Figure 9: A simulated rod antenna pattern for $R = 0.8$ m. The B-field is in mG.

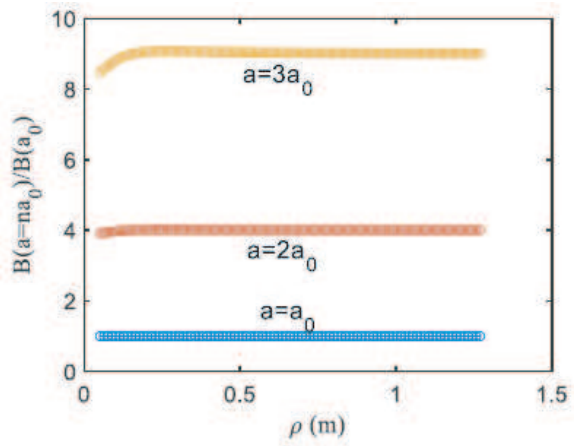

Figure 10: Influence of the antenna radius (a) on the B-field. The key parameters used are: $a_0 = 12.7$ mm, $z = 160$ mm. The other parameters are given in Table 1.

as the presence of wire mesh or large pieces of steel, can also cause changes in current which lead to a change in the B-field. Because of the linear relationship between I and B, the change of B caused by the variation of I can be conveniently compensated by a correction factor which is obtained by real time monitoring of the variation of the current I fed to the antenna. By doing so, it is anticipated that the performance degradation of a magnetic PDS caused by some of the environmental effects can be corrected.

Radius (a): Unlike the current I which has a strict linear relationship with B, how the antenna radius a relates to B is relatively more complicated. The analytical expression given in (10) reveals no apparent relationship between a and B. We numerically evaluate how B varies with the radius a by using (10). Specifically, the radius a is increased by a factor of n (i.e., $a = na_0$ where $n = 1$, 2, 3, and a_0 is the base radius) and the corresponding B for different radii are shown in Figure 10. For the sake of easy comparison, B values in Figure 10 have been normalized with respect to the B values of the reference case where the antenna radius is a_0. It is observed from Figure 10 that when an MWC is located at some reasonable distance away from the antenna (i.e., when ρ is large), B seems to be proportional to the square of the antenna radius. In other words, for a large ρ, the dependence of B on a can be summarized with the following formula:

$$B(\rho, z, a, N, L_c, I) \approx C_2(\rho, z, N, L_c, I) \cdot a^2 \tag{12}$$

where $C_2(\rho, z, N, L_c, I)$ is a constant that can be measured.

Number of Turns (N): Similarly, the dependence of B on the number of turns (N) of the antenna is evaluated based on (10) and the corresponding result is given in Figure 11. In this comparison, the B values have been normalized with respect to the B values of the reference case where the antenna has 10 turns. It can be found from Figure 11 that for a large ρ, B is proportional to N as described by the following formula:

$$B(\rho, z, a, N, L_c, I) \approx C_3(\rho, z, a, L_c, I) \cdot N \tag{13}$$

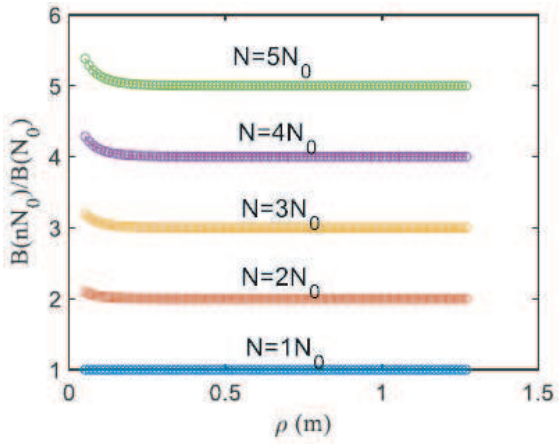

Figure 11: Influence of the number of turns (N) of the antenna on the B-field. The key parameters used are: $N_0 = 10$, $z = 80\,\text{mm}$. The other parameters are given in Table 1.

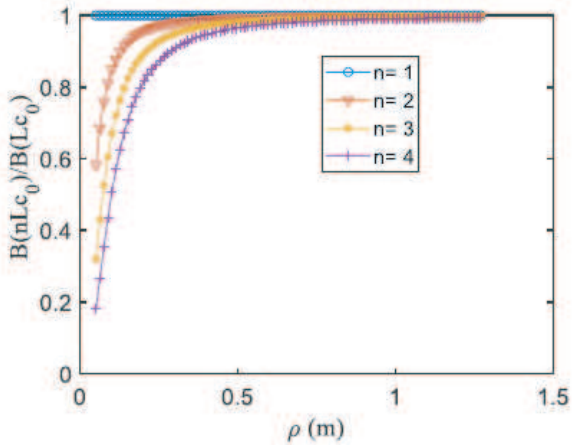

Figure 12: Influence of the coil length (L_c) on the B-field. ($a_0 = 12.7\,\text{mm}$, $z = 0$, and $Lc_0 = 80\,\text{mm}$). The other parameters are given in Table 1.

Coil length (L_c): Similarly, Figure 12 shows the dependence of B on the coil length. Interestingly, it is found that when an MWC is located at a relatively large distance from the antenna (about 0.5 m in this specific case) increasing the length of the antenna alone (without increasing the number of turns) doesn't gain too much as the B-field does not increase correspondingly. In addition, it is observed that for $\rho < 0.5$, the B-field for a longer antenna is actually smaller than that of a shorter antenna.

Permeability (μ_r): Since the analytical expression in (10) is only for an air coil, FEKO has been used for evaluating the dependence of B on the relative permeability μ_r of the ferrite core of the antenna. Figure 13 shows how B-field varies with μ_r. Again, for a better comparison, the B-field in Figure 13 has been normalized with respect to the B-field for the air coil case where

$\mu_r = 1$. It should be noted that the current of the antenna generally changes when μ_r is varied. To make the comparison fair, the B field has also been normalized with respect to the current to ensure the B field change in Figure 13 is caused by the variation of μ_r only. It is apparent that B dramatically increases with μ_r when μ_r is small and then saturates when μ_r reaches a value of close to 1000.

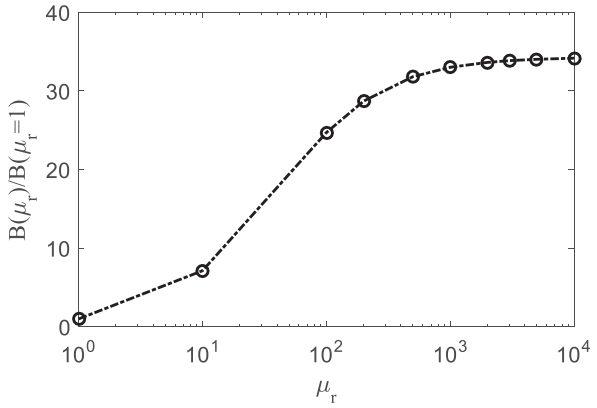

Figure 13: Influence of the relative permeability μ_r on the B-field.

Frequency (f): It is interesting to note that the B-field generated by an air coil seems to be independent of frequency as frequency is not included in the analytical model shown in (10). Although frequency is not a direct controlling factor, in reality, a change in frequency would likely cause the impedance of the antenna to change and thus a change in current. As a result, the B-field varies with frequency as well. Furthermore, the receiver generally requires one or sometimes multiple loop antennas to convert the received B-field to an electronic (typically, voltage) signal which is dependent on the frequency. In other words, even if the B-field generated by a PDS generator is independent of frequency, the receiver part (MWC) is frequency dependent, and thus the frequency has a direct impact on the performance of PDS.

6. CONCLUSION

A FEKO-based simulation approach is presented in this paper for modeling the B-field radiated from a PDS used for mining applications. It is shown that FEKO-based simulation results match well with analytical results and measurement results under various scenarios, indicating that FEKO can be used for accurately modeling the fields of a magnetic PDS. In addition, major parameters for controlling the performance of PDSs are analyzed. It is shown that the B-field from a PDS generator are mainly controlled by the current and the size of the antenna. Specifically, the vector sum of the B-field, which is the signal received by an MWC, is proportional to the current, and approximately proportional to the square of the antenna radius, as well as to the number of turns, when the MWC is at some distance away from the generator. The B-field dramatically increases with the relative permeability of the ferrite core when the relative permeability is small and generally saturates at a certain value, around 1000 for the specific case we investigated.

The FEKO-based simulation approach presented in this paper can be useful for investigating the dependence of environmental factors such as the presence of steel in the environment on the performance of a PDS, where physical measurements might be difficult to make. The findings of the paper will help researchers and PDS manufacturers to better understand the magnetic field coverage of PDSs and to design optimized PDSs that are more robust for underground mining environments.

ACKNOWLEDGMENT

The authors would like to acknowledge Nick Damiano, Jeff Yonkey, and Bruce Whisner for their help with taking the measurement data.

Disclaimer

The findings and conclusions in this report are those of the author(s) and do not necessarily represent the official position of the National Institute for Occupational Safety and Health (NIOSH),

Centers for Disease Control and Prevention (CDC). Mention of any company or product does not constitute endorsement by the NIOSH, CDC.

REFERENCES

1. MSHA, *Accident Injuries Data Set*, available: https://arlweb.msha.gov/OpenGovernmentData-/OGIMSHA.asp.
2. Carr, J. L., C. C. Jobes, and J. Li, "Development of a method to determine operator location using electromagnetic proximity detection," *2010 IEEE International Workshop on Robotic and Sensors Environments (ROSE)*, Phoenix, AZ, 2010.
3. Ducarme, J., J. Carr, and M. Reyes, "Smart sensing: The next generation," *Mining Magazine*, 58–66, 2013.
4. Jobes, C., J. Carr, and J. DuCarme, "Evaluation of an advanced proximity detection system for continuous mining machines," *International Journal of Applied Engineering Research*, Vol. 7, 649–671, 2012.
5. Bissert, P. T., J. P. DuCarme, C. C. Jobes, and J. D. Noll, "Alternate technologies applicable to proximity detection on mobile machines in underground coal mines," *The SME Annual Meeting, Denver*, CO, 2017.
6. Jobes, C., J. L. Carr, G. T. Homce, and A. K. Smith, "Analysis, conversion, and visualization of survey position and magnetic field strength data for a proximity detection system," *The SME Annual Meeting*, Phoenix, AZ, 2016.
7. Jobes, C., J. Carr, J. DuCarme, and J. Patts, "Determining proximity warning and action zones for a magnetic proximity detection system," *2011 IEEE Industry Applications Society Annual Meeting (IAS)*, Orlando, FL, 2011.
8. Carr, J. L. and J. P. DuCarme, "Performance of an intelligent proximity detection system for continuous mining machines," *The SME Annual Meeting*, Denver, CO, 2013.
9. Carr, J. L. and A. K. Smith, "Use of magnetic proximity detection systems in the presence of coal," *The SME Annual Meeting and Exhibit*, Denver, CO, 2013.
10. Carr, J. L., C. C. Jobes, T. J. Lutz, and J. A. Yonkey, "Underground field tests of second-generation proximity detection systems on continuous mining machines," *2015 SME Annual Meeting and Exhibit*, Denver, CO, 2015.
11. Carr, J. L., T. J. Lutz, and M. A. Reyes, "Field evaluations of proximity detection technology on continuous mining machines," *The SME Annual Meeting*, Salt Lake City, UT, 2014.
12. Li, J., J. Carr, and C. Jobes, "A shell-based magnetic field model for magnetic proximity detection systems," *Safety Science*, Vol. 50, 463–471, 2012.
13. Li, J., J. Carr, A. Smith, and J. Waynert, "A transferrable shell-based magnetic flux density distribution model for a magnetic proximity detection system," *2014 IEEE Industry Application Society Annual Meeting (IAS)*, Vancouver, Bristish Columbia, Canada, 2014.
14. Brocker, D., J. Waynert, P. E. Sieber, J. Li, D. H. Werner, and P. L. Werner, "Modeling of medium frequency propagation along a thin wire parallel to a lossy return path," *The 28th Annual Review of Progress in Applied Computational Electromagnetics (ACES)*, Columbus, OH, 2012.
15. Brocker, D. E., P. L. Werner, D. H. Werner, J. Waynert, J. Li, and N. W. Damiano, "Characterization of medium frequency propagation on a twin-lead transmission line with earth return," *2012 IEEE Antennas and Propagation Society International Symposium (APSURSI)*, Chicago, IL, 2012.
16. Brocker, D. E., P. E. Sieber, J. A. Waynert, J. Li, P. L. Werner, and D. H. Werner, "A hybrid approach for efficient modeling of medium-frequency propagation in coal mines," *IEEE Antennas and Propagation Magazine*, Vol. 57, 164–176, 2015.
17. Brocker, D. E., P. L. Werner, D. H. Werner, J. Waynert, J. Li, and N. W. Damiano, "Multimode propagation on a medium frequency twin-lead transmission line with earth return," *2013 IEEE Antennas and Propagation Society International Symposium (APSURSI)*, Orlando, FL, 2013.
18. Yan, L., J. Waynert, and C. Sunderman, "Measurements and modeling of through-the-earth communications for coal mines," *2012 IEEE Industry Applications Society Annual Meeting (IAS)*, Las Vegas, NV, 2012.
19. Jackson, J. D., *Classical Electrodynamics*, John Wiley & Sons, Inc., New York, NY, 1999.
20. Smythe, W. B., *Static and Dynamic Electricity*, Hemisphere Publ. Corp., 1988.

21. Stadler, A., "Radiated magnetic field of a low-frequency ferrite rod antenna," *2011 7th International Conference-Workshop, Compatibility and Power Electronics (CPE)*, 283–288, 2011.
22. Callaghan, E. E. and S. H. Maslen, "The magnetic field of a finite solenoid," NASA Lewis Research Center Tech Note D-465, 1960.

